ANNALS OF GEOPHYSICS, 68, 5, DM575, 2025; doi:10.4401/ag-9384
OPEN ACCESS

SantoArray: A dense hybrid temporary network in the Santorini volcanic complex for seismic monitoring and study of its crustal structure

Konstantinos Gkogkas[*,1], Costas Papazachos[2], Nikos Chatzis[2], Chrisa Ventouzi[2], Domenikos Vamvakaris[2], Eleni Karagianni[2], Parthena Paradisopoulou[2], Alexandros Vellis[2], Nikos Anterriotis-Kalpakidis[2], Dimitrios Madelis[2], Elina Aidona[2], Christos Pikridas[2], Charalampos Kkallas[2], Wojciech Czuba[1], Monika Bociarska[1]

(1) Institute of Geophysics, Polish Academy of Sciences, Warsaw, Poland
(2) Aristotle University of Thessaloniki, Thessaloniki, Greece

Article history: received June 14, 2025; accepted November 6, 2025

Abstract

SantoArray, a dense temporary land seismic network, was deployed in the Santorini volcanic complex from February 28 to March 23, 2025, in response to the 2024-2025 Santorini-Amorgos intense volcano-tectonic unrest which included a significant earthquake sequence with more than 10 events with $M_L \geq 5$. The network consisted of 117 DATA-CUBE 3-component digitizers with 4.5 Hz geophones, complemented by 7 SmartSolo 5 Hz sensors and 12 permanent wideband and broadband stations. It operated in two phases with varying configurations, achieving an average ~0.6 km inter-station spacing in Phase II, with more than 98% of data recovery during its operation. Preliminary analyses of P-wave travel-time mapping from intra-caldera and regional earthquakes suggests that the network data can significantly improve hypocentral accuracy especially within the caldera. Moreover, ambient noise spectra, HVSR and cross-correlation analysis reveals important information on the volcanic thickness variations above the metamorphic basement, resulting in high amplifications of strong ground motions. The analysis suggests that this large-N array provides a robust dataset for advanced tomographic imaging, enhancing the resolution of Santorini's shallow crustal structure and seismicity using ambient noise and earthquake waveform data. The retrieved information can offer critical insights into the 2025 unrest and Santorini's subsurface dynamics, allowing us to improve seismic hazard assessment for the Santorini volcanic complex.

Keywords: Santorini Volcano; Seismic Hazard; Volcano-Tectonic Seismicity; Earthquake Relocation; Ambient Noise; HVSR; Cross-Correlation; Near-Surface Structure

1. Introduction

The Santorini island, located in the southern Cyclades complex, is considered as the most active volcano of the Hellenic Volcanic Arc. The subduction of the Eastern Mediterranean plate beneath the Aegean microplate

(Papazachos and Comninakis, 1969, 1971; Caputo et al., 1970; Le Pichon and Angelier, 1979) and its associated rollback have generated the ongoing extension phase of the Aegean (Bohnhoff et al., 2006), as well as the volcanism of the Hellenic Volcanic Arc which migrated its present position since the Miocene (Fytikas et al., 1984). The main tectonic structures of the southern Cyclades consist of large tectonic horsts and grabens, which were mainly formed by the NW-SE Miocene extensional field (e.g. Hooft et al., 2017; Nomikou et al., 2018; Heath et al., 2019; Tsampouraki-Kraounaki et al., 2021). The broader Santorini-Amorgos area (Fig. 1a) is also characterized by significant seismotectonic activity as evidenced by the 1956 M7.5 earthquake (e.g. Papadopoulos and Pavlides, 1992; Okal et al., 2009; Konstantinou, 2010; Brüstle et al., 2014) which was the largest crustal earthquake of the last two centuries in Europe. This mainshock caused moderate-to-heavy damage (Modified Mercalli intensities 7 and larger) in Santorini and the surrounding Cyclades islands (Papazachos and Papazachou, 2003).

As can be seen from the simplified geological map of Santorini island presented in Fig. 1b, the broader area is dominated by volcanic deposits, resulting from the intense volcanic activity started ~650 ka ago (e.g. Druitt et al., 1999), above the typical metamorphic basement of the Cyclades. This metamorphic basement crops out in the central-southern part of Santorini (pink units in Fig. 1b) and consists of Cenozoic schists and Mesozoic crystalline limestones (e.g. Skarpelis and Liati, 1990). According to Druitt et al. (1999) the volcanic formations are composed of hundreds of meters of pyroclastic deposits and lava flows. The oldest volcanic products (340-650 ka) are located on the Akrotiri Peninsula in the south-eastern part of Santorini (see Fig. 1b) and mainly consist of lava flows. Following this initial volcanic activity, at least 11 Plinian or larger eruptions have occurred during the first (180-360 ka) and the second (22-180 ka) explosive cycles, producing extensive pyroclastic deposits and lava flows over Santorini (black units in Fig. 1b).

Roughly 3.6 ka ago, the second explosive cycle ended with a major Plinian eruption during the Late Bronze Age (~1560 BCE; Ehrlich et al., 2021), referred to as the LBA Minoan eruption. This eruption produced extended pyroclastic deposits of tuffs (Phases 1-3) and ignimbrites (Phase 4), which have covered the largest part of Santorini (e.g. Druit et al., 2019) and are depicted in Fig. 1b as yellow and green units, respectively. At least 5 collapse episodes have occurred during these two explosive cycles, which contributed to the formation of the present-day Santorini caldera. Recent volcanic activity has continued from 197 BCE to the present, producing dacitic lavas that formed the Palea and Nea Kameni islets in the centre of the Santorini caldera (e.g. Vougioukalakis and Fytikas, 2005; Pyle and Elliot, 2006), along the intra-caldera Kameni line. Following the latest 20th century volcanic activity in 1950 (Georgalas, 1953), a significant volcano-tectonic unrest occurred in 2011-2012, with a low-magnitude seismic swarm along the Kameni line (Tassi et al., 2013; Papadimitriou et al., 2015) and radial caldera extension and uplift (Newman et al., 2012; Foumelis et al., 2013; Parks et al., 2013, 2015).

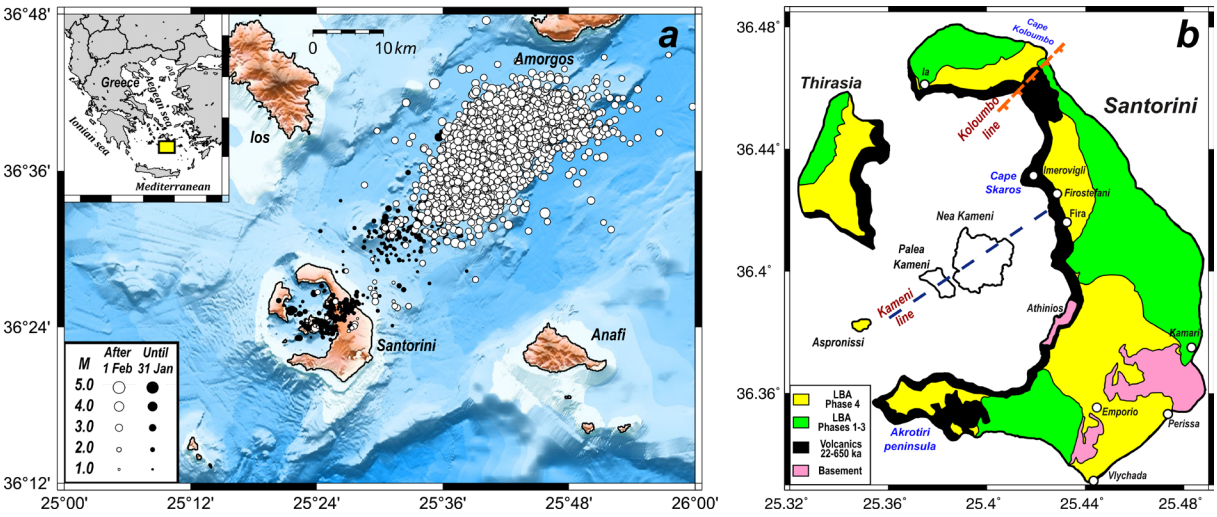

Figure 1. (a) Map of the broader Santorini island area (see inset figure for geographical context). The seismicity related to the 2024-2025 intra-caldera unrest (till 31 Jan 2025) and the 2025 Santorini-Anydros-Amorgos volcano-tectonic crisis (after 1 Feb 2025) is also presented. (b) Simplified geologic map of Santorini volcanic complex (after Flaherty et al., 2018). Major municipalities and landmarks, as well as the two principal seismotectonic lineaments (names outlined with red text) within the island are also depicted.

Since mid-summer of 2024 a complex and intense volcano-tectonic unrest has occurred in the broader Santorini area (Fig. 1a). Its first phase (till late January 2025) involved an intra-caldera volcanotectonic unrest similar to 2011-2012, with a low-magnitude seismic swarm mainly along the Kameni line (black circles in Fig. 1a), as well as a similar deformation pattern due to the intrusion of 6+ million m^3 at a depth of ~3.5 km in the northern Santorini caldera (Papazachos et al., 2025). This activity was followed by a more intense, larger magnitude, seismic swarm, which occurred between Santorini and Amorgos, with thousands of earthquakes being recorded in February and March 2025, with a maximum magnitude of M5.2 (e.g. Huftstetler et al., 2025). Hundreds of earthquakes with magnitudes larger than 3 were felt by inhabitants of Santorini and neighbouring islands, leading to a tentative self-evacuation of Santorini and the declaration of emergency state by the Hellenic government. In light of these events, we rapidly responded to the ongoing crisis by designing and deploying a new seismic array in Santorini (SantoArray). The collaboration between the Aristotle University of Thessaloniki (Greece) and the Institute of Geophysics, Polish Academy of Sciences (Poland) facilitated the preparation, shipment, deployment, maintenance, and data analysis of 7 SmartSolo units and 117 DATA-CUBE instruments equiped with HG (Bcoil) 4.5 Hz geophones (9090 Ohm shunt for damping and effective sensitivity of 27.7 V/m/s). The network operated continuously for approximately 3.5 weeks (28 February-23 March 2025) without instrumentation losses, resulting in a substantial volume of data recorded by the deployed large-N array. We present detailed information on this newly deployed temporary seismic network along with a preliminary example of data analysis.

2. The SantoArray network and performance

The SantoArray comprises of continuous records from all permanent (broadband and wide-band; red squares in Fig. 2) stations in Santorini operating under the Hellenic Unified Seismic Network (H.U.S.N., Evangelidis et al., 2021), augmented with temporarily deployed nodal stations (117 DATA-CUBE 3-C and 7 SmartSolo 3-C instruments) in two deployment phases (I and II), with distinct instrument configurations and geometries. Phase I (28 February-11 March, Fig. 2a) involved the installation of 7 SmartSolo 5 Hz with IGU-16HR-3C sensors (blue triangles in Fig. 2) and 117 DATA-CUBE digitizers equipped with HG-6B 4.5 Hz 3-component sensors. DATA-CUBES were set in two different instrument gain configurations (minimum – "low" with a gain amplification of 1, i.e. 244.14 nV/count and maximum – "highest" possible with an amplification factor of 64, i.e. 3.815 nV/count) deployed as follows: 50 co-located low- and high-gain sensor sites (grey triangles in Fig. 2a), 10 high-gain sensors (white triangles in Fig. 2a) and 7 low-gain sensors (black triangles in Fig. 2a), with a ~1.3 km average inter-station spacing. Phase II (11-23 March; Fig. 2b) was initiated due to instrument battery (2 PROCELL intense D-size 1.5 V batteries, with a total nominal capacity of 37.2 Ah) replacing needs and comprises of the same total instrument number. However, during Phase II we have set all sensors configuration to the maximum possible gain (white triangles in Fig. 2a), while sensors co-located at "double" (low- and high-gain) sites and near permanent station locations (grey and several black triangles of Fig. 2a) were relocated and distributed throughout Santorini to ameliorate the inter-station spacing to about 600 m. We chose these instrument amplification gain and instrument geometry phases for two reasons: (1) to avoid clipping of seismic records in case of large magnitude event during Phase I, (2) since the sequence was de-escalating, to record low amplitude seismic noise and create station grid more suitable for seismic tomography during Phase II.

Field work was carried out during three (3) visits: one for the initial deployment (Phase I), one for the change of batteries/relocation (Phase II), and one for the instrument retrieval. Intra-continental shipping of 117 CUBE stations between Warsaw, Poland and Santorini, Greece was achieved within 1 week one-way. Stations were installed based on a preliminary installation grid plan (~1.3 km spacing for Phase I and ~0.6 km for Phase II), which also considered the locations for which previous ambient noise measurements have been performed in the island (Fig. 2b), as these were compiled by Chatzis et al. (2022). Most of the sites were selected in rural locations and both sensors and digitizers were typically buried at ~0.5 m below the ground (Fig. 3a). We chose to deploy co-located stations with low- and high-gain sensors during Phase I to avoid any potential recording clipping from very strong events of the ongoing Santorini-Amorgos seismic sequence. The final station locations were determined based on the site availability and minimum disturbance from anthropogenic activities (Fig. 3b). Transportation to Thirasia and Kameni was achieved through boat rides operating on a regular basis with instruments sealed in metal boxes (Fig. 3c). In total, 3 to 4 teams of 2 people participated at each stage for about 2-3 days total trip duration. The workload in Santorini was distributed between in 3 areas (South, Central, North) and installations finished within 1-2 days. Similarly, transportation and instrumentation in Thirasia and Nea Kameni islands took 1 day to complete.

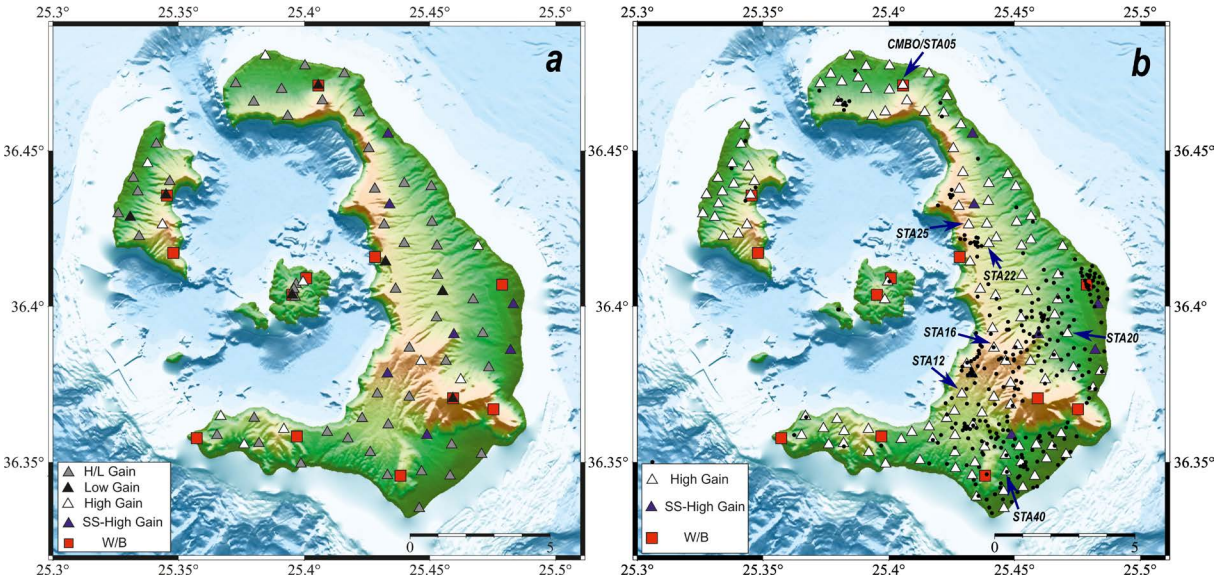

Figure 2. (a-b) Phase I and II, respectively, of the Santo Array sensor distribution (blue triangles: 7 SmartSolo sensors, black/grey/white triangles: 117 DATA-CUBE sensors). Previous HVSR measurements are shown with black dots. SantoArray stations for which data usage examples are presented in the main text are annotated. Red squares show operating permanent Wideband or Broadband stations from the Hellenic Unified Seismic Network (H.U.S.N.).

The overall array deployment and operation was a success with all stations successfully recovered and above 98% expected data retrieval. Site disturbances were minimal with only 2 reported cases of ad-hoc instrument relocation due to human activity. Despite the cautious station burial below the ground, several stations lost GPS signal at rather irregular times (1 during Phase I and 7 during Phase II), most likely due to intense rainfalls occurring during the second stage of the experiment. We cross-validated the station coordinates based on field

Figure 3. Example field site installations: (a) Typical sensor and DATA-CUBE placement, (b) Station STA40 site deployed in the Vlychada-Perissa area (see Fig. 2b), (c) Boat transportation of instrument boxes to the Thirasia and Nea Kameni islands.

notes and GPS locations (when applicable) to an accuracy of ~1 m. Moreover, as poor GPS signal may result in clock synchronization issues, we have determined the time gaps where particular (<10) stations lost reliable satellite connection (typically for a few hours, usually not exceeding ~2 days). Notice that the instruments perform a linear clock drift correction whenever they retrieve GPS signal. Moreover, we have updated the station metadata, in order to maintain the option to reject data that depend on accurate timing (e.g. event relocation, travel-time tomography, etc.), to avoid challenges in future research.

It is interesting to study the noise records of the instruments employed in SantoArray, as this reveals valuable information regarding the ambient noise wavefield characteristics (e.g. retrievable spectra, anthropogenic noise levels, etc.) recorded by SantoArray. For this reason, we present in Fig. 4 three comparisons of the noise Power Spectral Density (PSD) from the experiment. Figure 4a depicts a PSD comparison of a collocated low- and high-gain DATACUBE digitizers with 4.5 Hz sensors during Phase I (station STA22, see Fig. 2b for location of all stations mentioned hereinafter) for a day (8 March 2025), which was rather "quiet" (no rain, weak winds and sea waves, etc.). The recovered PSD information shows very good agreement in the range 2-40 Hz, with an adequate agreement down to ~0.6 Hz, which is quite exciting since a 4.5 Hz geophone was used in both cases. At lower frequencies the low-gain PSD (black line) is dominated by instrument noise, increasing significantly at lower frequencies.

The presented PSD beheavior is typical for all low-gain instruments used in the experiment. In Fig. 4b we present the HVSR curve (Nakamura, 1989) for the records of Fig. 4a. Since this station was located at a site with thick volcanic deposits (e.g. locally exceeding 1 km, Heath et al., 2019) a clear low fundamental frequency, f_0, peak is identified at ~0.35 Hz for the high-gain sensor, with significant peak HVSR amplitude (A_0^{HVSR}~3.5), in agreement with previous HVSR data in the broader area (Chatzis et al., 2022). Since this peak fall outside the frequency range for which the low-gain sensor is properly recording ambient noise (<0.6 Hz), the corresponding peak is practically not recognized. In such cases, using the low-gain sensor HVSR curve would lead to a misidentification of the second HVSR peak (~0.6-0.7 Hz) as structural information.

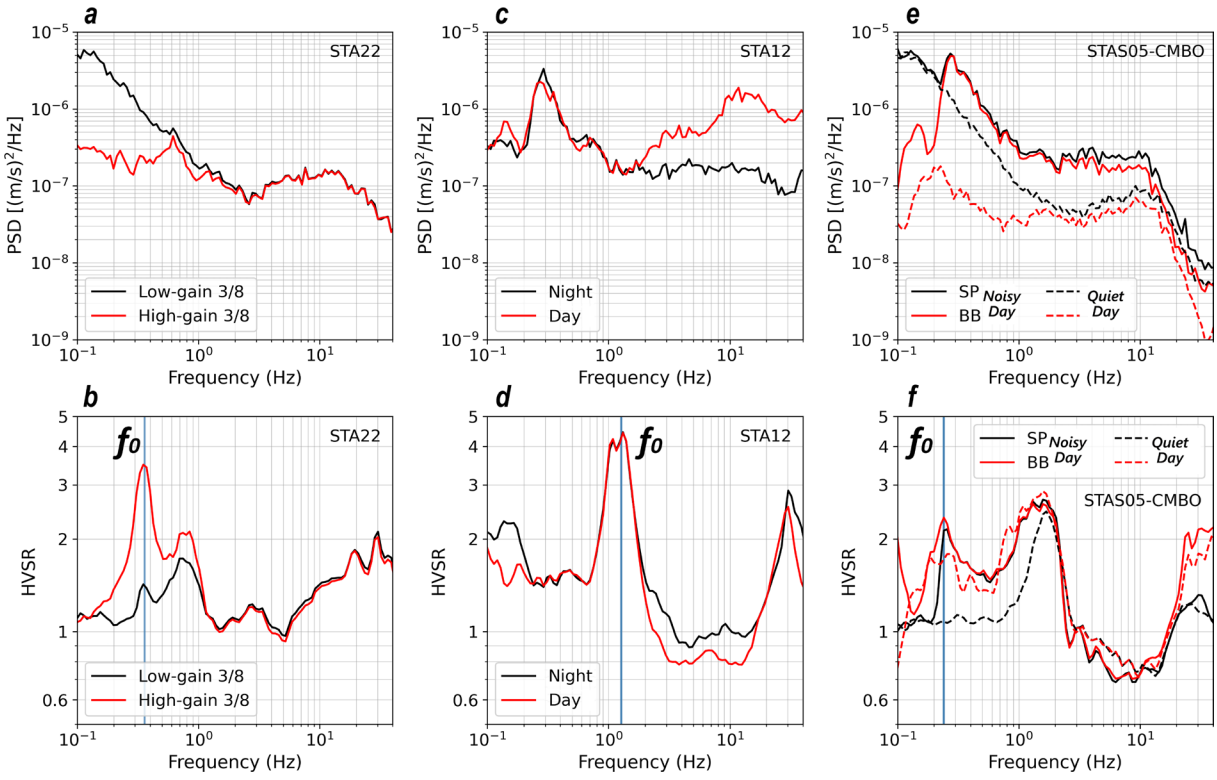

Figure 4. Vertical component ambient noise Power Spectral Density (PSD) plots for different instruments and configurations (a, c, e) and corresponding HVSR mean curves (b, d, f) for the SantoArray network: (a and b) Low- versus High-gain 4.5 Hz DATA CUBE 3-C data for station STA22. (c and d) High-gain DATA CUBE data for noisy (day) and quiet (night) time windows (station STA12). (e and f) Comparison of data from the permanent broadband station CMBO and the nearly co-located low-gain DATA CUBE sensor (STAS05). The fundamental frequency for all stations, f_0, is depicted in the HVSR plots with a vertical solid line (see text for details).

The high levels of environmental or urban noise (e.g. due to traffic) did not seem to significantly affect the recorded ambient noise wavefield. This is demonstrated at Figs. 4c and 4d where we present the ambient noise PSD and HVSR curves, respectively, for "noisy" (mainly during the day) and "quiet" (mainly during the night) time windows of the high-gain sensor at an example station leading to a higher fundamental frequency (f_0~1 Hz) due to the proximity to the bedrock. The derived f_0 and A_0^{HVSR} values are consistent for both time windows, with subtle differences observed in the HVSR amplitude at low- and high-frequency (anthropogenic) bands, despite the much larger ambient noise level observed during the day for frequencies above ~2 Hz.

Finally, in Fig. 4e we compare a low-gain sensor (STAS05, see Fig. 2b) and the nearly co-located broad-band permanent station CMBO (close to Cape Koloumbo, Santorini, see Fig. 1b), equipped with a Nanometrics Trillium 120P sensor. Even though both sensors were installed on andesite, the broader area is characterized by the presence of a very thick volcanic deposits layer above the metamorphic basement (Heath et al., 2019; Chatzis et al., 2022), leading to a very low fundamental frequency (f_0~0.25 Hz). We present data for a "quiet" day (4 March 2025-low ambient noise levels), as well as a "noisy" day (10 March 2025, exacerbated natural activity due to strong rain and winds). For the "noisy" day both instruments resolve the fundamental frequency and the peak HVSR amplitude consistently (Fig. 4f), as the ambient noise PSD level is above the instrument noise down to ~0.22 Hz as shown by the CMBO-STAS05 PSD comparison in Fig. 4e. On the contrary, during the "quiet" day the low-gain ambient noise PSD is mainly controlled by the instrument internal noise, showing a pattern akin Fig. 4a with high ambiguity below ~1.5 Hz. On the contrary, during the "noisy" day, the high-level of ambient noise allows the sensor to reliably record the ambient noise wavefield down to ~0.25 Hz, as can be also seen by the comparison with the CMBO broadband sensor. These observations showcase the spectral content confidence of our new array and underscore the nodal instrument potential to retrieve signals much lower than their cut-off frequency, contrary to suggestions that typically discourage their usage for shallow crustal studies compared to higher-cost broad-band sensors. We illustrate the poor low-frequency performance of low-gain sensors, which is not surprising as the digitizers gain intrinsically controls the instrument's ability to display the small amplitudes typifying slow motions (low frequency/long-period).

3. SantoArray data usage examples and discussion

Figure 5 presents a preliminary analysis of two local earthquakes that occurred in the Santorini volcanic island (2025/03/20 M2.5, original and relocated hypocenter also shown in Fig. 5a) and the Santorini-Amorgos area, occuring outside of the network (2025/03/21 M4.7, Fig. 5b) and recorded during second phase of the SantoArray experiment operation (Phase II). For both events, P- and S-wave phases were manually picked, and P-wave arrival times were calculated relative to the origin time of each event. We then applied a simple topographic correction to account for the rapidly changing topography in Santorini, incorporating a mean P velocity determined from the average S velocity estimated by Chatzis et al. (2022) using the empirical relationship of Brocher (2005). A smooth 2D kriging interpolation was applied to the observations to enhance the visualization of the spatial wave propagation. The preliminary travel-time surfaces completeness verifies the adequate data quality and density for earthquakes occurring both inside the Santorini caldera (Fig. 5a), as well as outside the caldera (Fig. 5b) from Santorini. The resulting maps are coherent with a large number of stations providing high quality data and changes in the time contours (i.e. deformation of wave-field) provide direct information about structural (velocity) changes in Fig. 5b. Differences in time arrivals highlight the possible presence of loose formations (sparse time contours in Fig. 5b) and near the bedrock (dense time contours in Fig. 5b).

The focal parameters of the two earthquakes in Fig. 5 were determined using the Hypoinverse software (Klein, 2002). For the intra-caldera earthquake, we employed two different approaches: Initially, only data from the permanent seismic network of Santorini were used. Subsequently, the calculation was repeated by incorporating all manually picked phases from SantoArray network as well. The two resulting epicentral locations, based on the different number of phase readings, are illustrated in Fig. 5a using a large light blue circle (permanent network only) and a smaller red circle (combined permanent and temporary stations, i.e. the full experimental dataset). These colored areas represent the 1-sigma horizontal location uncertainty (ERH) region when using the permanent network alone, and when using the complete SantoArray P and S phase dataset, respectively. The difference in location uncertainty is evident, with the inclusion of the full dataset significantly improving the accuracy of the hypocentral parameter estimates for earthquakes occurring within the broader area of the Santorini caldera volcanic complex.

One primal research direction for the SantoArray ambient noise data is related to the determination of the volcanic layer thickness in the islands via the determination of the fundamental frequencies (f_0) and amplitudes (A_0) of ambient noise recordings. Previous results on this topic (Chatzis et al., 2022) focused mainly on central Santorini presenting fundamental frequency, f_0, spatial variation in good correlation with local geology, while revealed large maximum HVSR amplitudes (A_0^{HVSR}), indicating possible signifcant ground motion amplifications due to site-effects. To explore this issue, we calculated preliminary HVSR curves using all available high-gain stations from SantoArray Phase I. We employed the Geopsy software package (Wathelet et al., 2020) to calculate HVSR curves for 10-minute time windows and for a total duration of 1 day per each station. We automated the process using the procedure described in Chatzis et al. (2022) and manually inspected the results to ensure high quality. In Fig. 6, we present two examples of HVSR curves obtained from single-station 3 component ambient noise measurement at two sites located relatively close to and at a large distance from the outcropping basement. The results verify the presence of a thin at the first site (f_0~1.5 Hz) and a thick at the second site (f_0~0.35 Hz) volcanic layer deposits above the metamorphic basement. Both plots indicate the presence of high A_0^{HVSR} values, in agreement with previous results in the area.

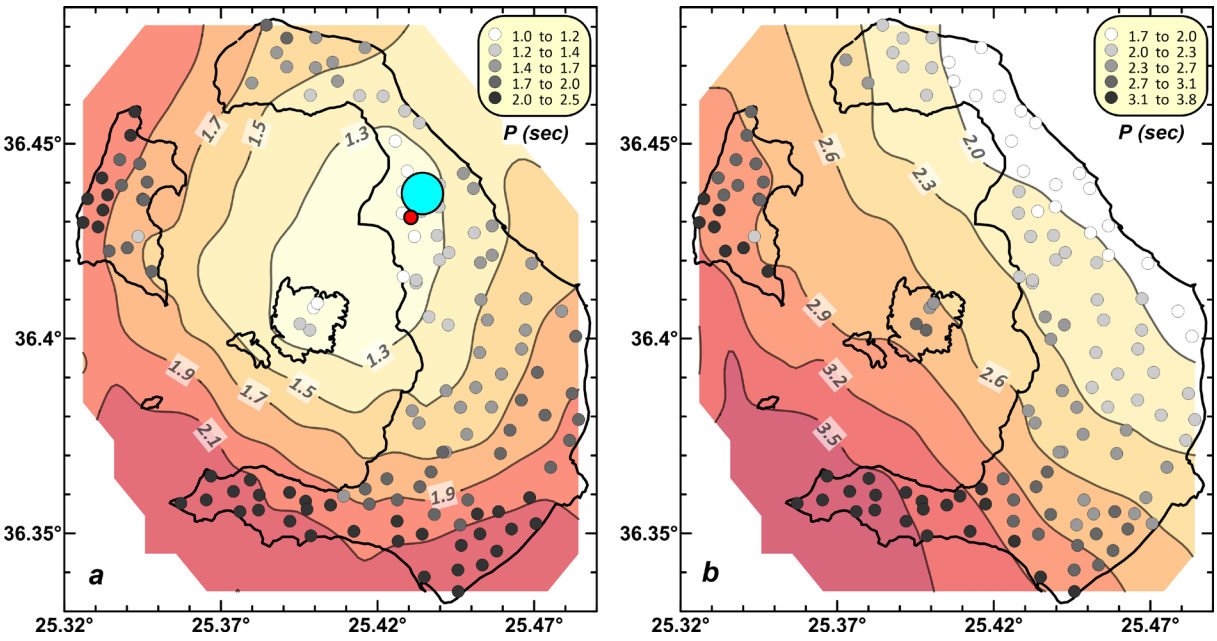

Figure 5. Example of P-wave arrivals (colored circles) for two earthquakes of the Santorini-Amorgos seismic sequence recorded by SantoArray (Phase II), as picked on the vertical component and corrected for topography using an average V_P of 2.8 km/s. Smoothed arrival contours are also plotted for both figures: (a) P-wave travel-times for the 2025/03/20 M2.5 intra-caldera earthquake. The light blue and red circles depict the 1-sigma horizontal uncertainty locations using only the permanent network data and the complete SantoArray P and S arrivals, respectively, resulting in a much smaller location error in the second case. (b) Same plot for the arrivals of the 2025/03/21 M4.1 Santorini-Anydros-Amorgos sequence event (relative to an arbitrary reference time – see text for details).

To further explore the potential of SantoArray to provide reliable and high resolution near-surface structural constraints from single station analysis, we present the obtained fundamental periods (T_0) spatial distribution (Fig. 7a) and peak ground amplifications (A_0^{HVSR}) from the HVSR data of SantoArray Phase I (Fig. 7b) compared to results from previous deployments (Chatzis et al., 2022). The new HVSR results are in excellent agreement with previous analyses and exhibit the expected volcanic layer thickening with finer detail as we move away from the metamorphic bedrock near Profitis Ilias. Specifically, the HVSR curves manifest low T_0 values (<0.4 s) and very low A_0^{HVSR} (<2.5) or relatively flat shapes over the outcropping limestone basement of Profitis Ilias mountain, typical for bedrock sites. Moreover, prominent frequency peaks at 1.25-2.5 Hz (T_0 = 0.4-0.8 sec) with very high A_0^{HVSR} values (4-10, e.g. Fig. 6a) are identified in the vicinity of Profitis Ilias across the broader Megalochori, Perissa and Kamari basins (west, south and north of the Profitis Ilias basement, respectively), emerging from the high-impedance

contrast between pyroclastics (mainly Minoan deposits) and the basement (Chatzis et al., 2022). These pyroclastic deposits above the basement can be directly observed along the Caldera wall at the Athinios site (see Fig. 1) with an average total thickness of ~130 m. A significant increase in the fundamental period is clearly identified from the broader Profitis Ilias bedrock area toward the northern (Fira) and eastern (Akrotiri) parts of the island, due

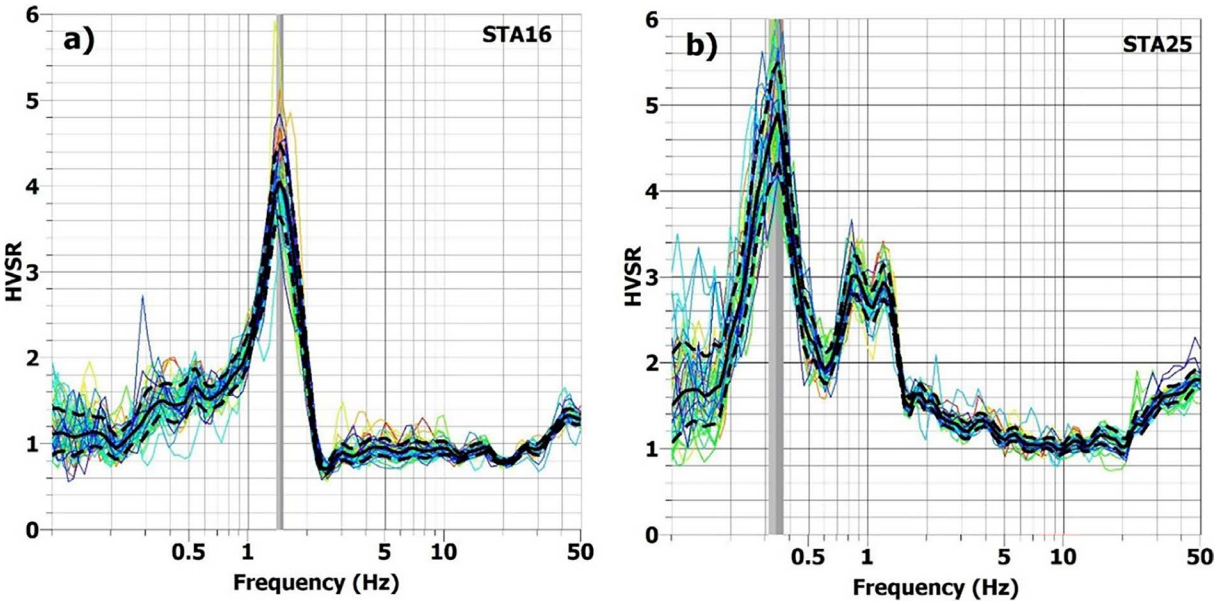

Figure 6. Typical HVSR curves for two sites with different geological settings (fundamental frequency and its uncertainty are depicted with a vertical grey bar): (a) Station STA16 located close to a metamorphic basement outcrop, with a fundamental frequency at $f_0 \simeq 1.5$ Hz and a prominent single peak due to impedance contrast between pyroclastic deposits and the underlying basement. (b) Station STA25, showing a very low fundamental frequency ($f_0 \simeq 0.35$ Hz), indicative of very thick volcanic deposits (several hundreds of meters) above the basement. Secondary peaks near $f_1 \sim 1$ Hz are also recognized, possibly due to a shallower impedance contrast within the volcanic layers.

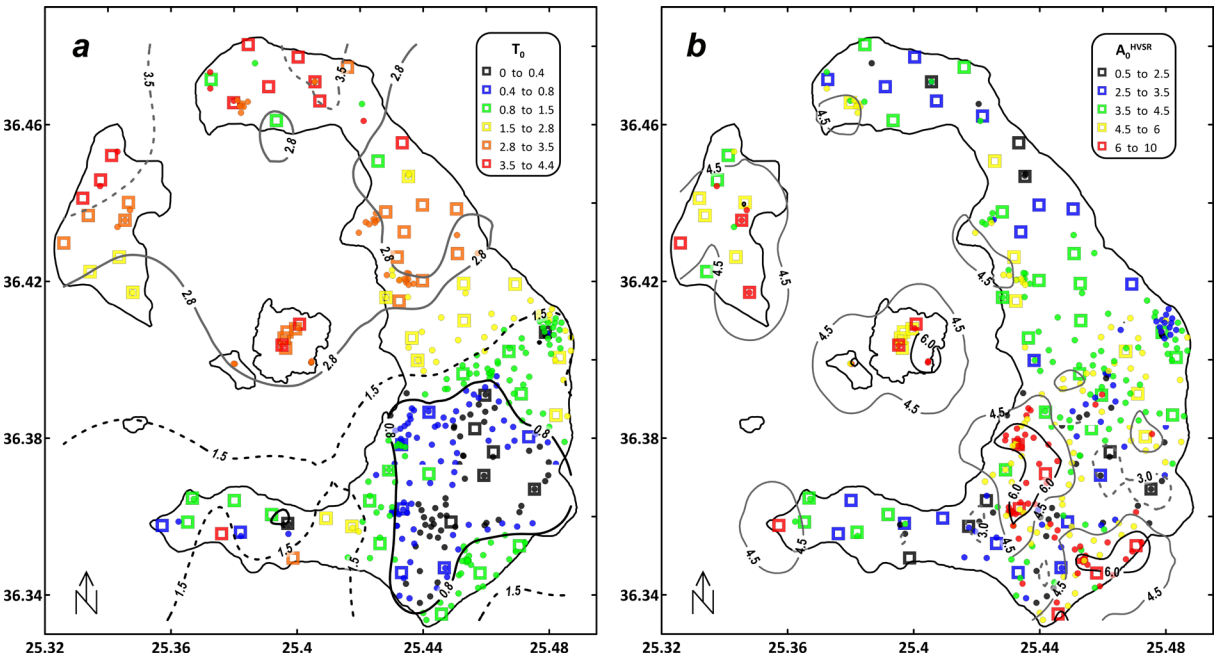

Figure 7. Spatial variation of the fundamental period (T_0, left) and corresponding HVSR amplitudes (A_0^{HVSR}, right) determined from ambient noise data from previous studies (filled circles, Chatzis et al., 2022) and SantoArray sensors (open squares). Smoothed contours indicating the spatial variation are also plotted in both figures.

to the increased thickness of volcanic deposits. Furthermore, more complex structures are present in Fira and Akrotiri areas, where interbedded lava flows likely exist within the pyroclastic deposits. These lavas result in the overall reduction of the A_0^{HVSR} values and generate secondary, shallower impedance contrasts, as well as additional frequency peaks in the HVSR curves (e.g. f_1 peak in Fig. 6b). Large T_0 values (~3 sec) are also observed for the remaining part of the volcanic complex in Nea Kameni and Thirasia islets, as well as the northern Santorini (close to Ia) areas, verifying the presence of a deeper basin filled with volcanic material (Heath et al., 2019).

To examine the ambient-noise imaging aptitude of SantoArray, we calculated the cross-correlation functions based on the methodology outlined in Lin et al. (2012). The instrument response is removed, and the data are de-meaned, de-trended and cut into daily segments. We then apply temporal normalization to effectively suppress earthquakes and spurious signals (e.g. spikes) from the time series and spectral whitening to broaden the ambient-noise signal energetic band and evenly enhance low and high frequencies. Figure 8 shows an example of 9-component cross-correlations between virtual source station high-gain sensor STA20 (Fig. 2b) to all SantoArray high-gain sensors and permanent stations, rotated from ZNE to the ZRT coordinate system and band-passed

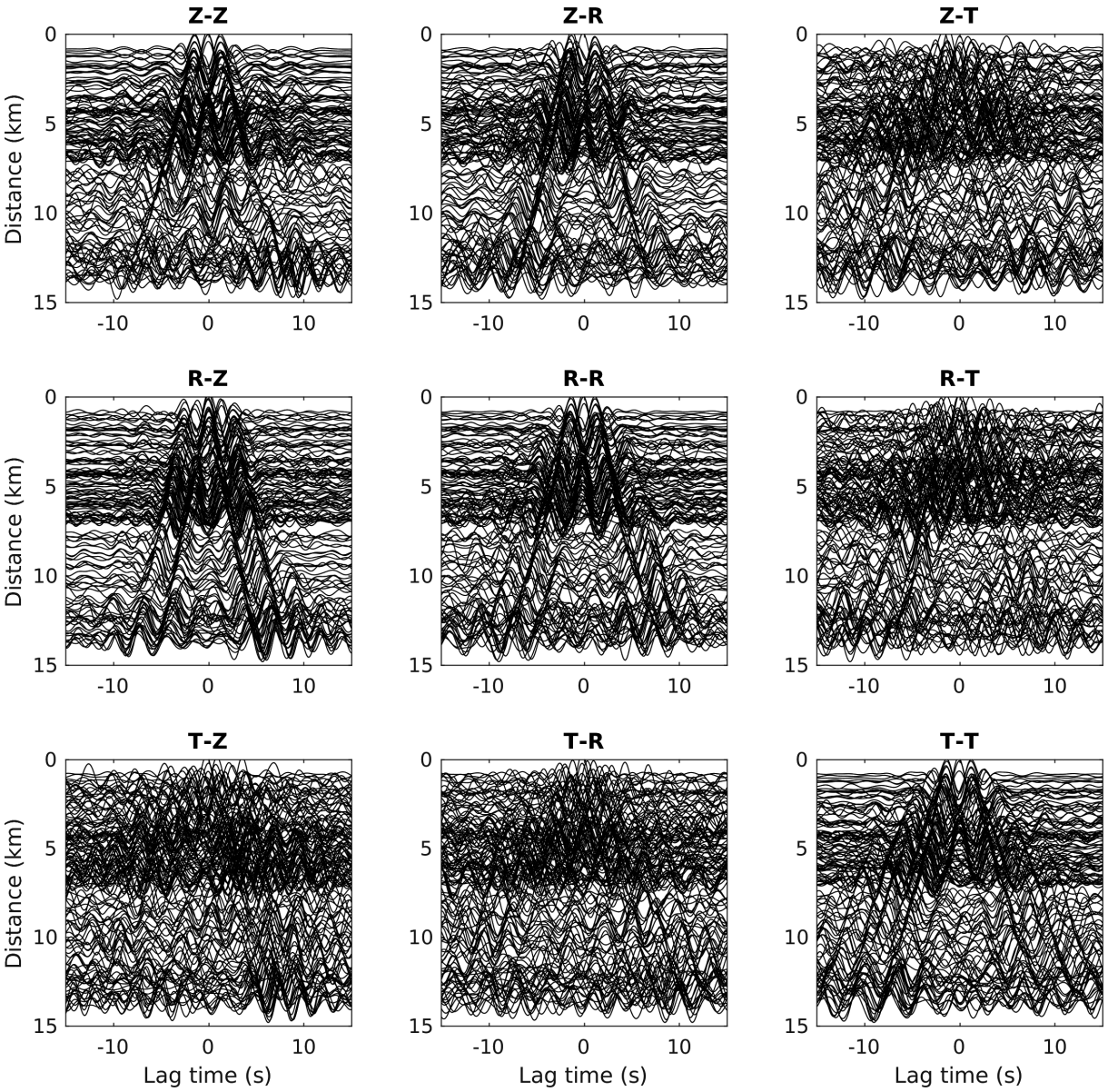

Figure 8. Ambient-noise cross-correlations: The 9-component cross-correlation tensor (Z: Vertical, R: Radial, T: Transverse; Z-Z, Z-R, Z-T, R-Z, R-R, R-T, T-Z, T-R, T-T) between virtual source station STA20 and all possible high gain array receivers and permanent stations, band-passed in the range 2-4 s. Clear Rayleigh (Z-Z, Z-R, R-Z, R-R) and Love (T-T) wave signal moveouts are observed.

in the range 2-4 s periods. Clear Love (T-T component) and Rayleigh wave signal move-out is observed (Z-Z, Z-R, R-Z, R-R components).

Figure 9 depicts an example Frequency-Time Analysis (FTAN) diagram, where the correlogram between stations STA20-STA25 is band-passed near different central periods, and the normalized signal envelope is plotted versus the linked group velocity. The FTAN diagram shows the correlogram fine-detail spectral content, where the continuous surface wave dispersion curve can easily be determined between ~1-3.5 s periods. Moreover, a rapid velocity increase is observed from 0.3 km/s to 1.2 km/s within periods of 1-3.2 s, indicative of the strong velocity contrast between shallow volcanic layers and the metamorphic basement. Longer period signal measurement naturally requires longer distances than the SantoArray aperture (~15 km maximum inter-station distance) to satisfy the far-field approximation (e.g. Yao et al., 2006) and regional H.U.S.N. stations will be considered in the future for deeper structure analysis. Short periods/high frequencies, while retrievable (see Figs. 4 and 9), attenuate faster with distance and dispersion curve continuity will be intensified through phase-association.

Our ambient-noise imaging efforts will aim towards computing the period-dependent surface wave phase velocity via the tomographic inversion (e.g. Wang et al., 2017; Hannemann et al., 2014) of acquired path surface wave averaged travel-times (Fig. 9) and/or beamforming techniques (e.g. Gkogkas et al., 2021) to enhance the signal prior to measuring local 1-D dispersion curves. The joint inversion of the new high-resolution 1-D local phase velocities with independent datasets will illuminate the architecture and the mechanical properties of shallow crustal stratigraphic formations through velocity gradients in the top ~5 km with unprecedented resolution. While most common surface wave tomography practices resolve only the shear wave velocity, joint inversions of different geophysical datasets can also provide information about the density (through gravity, e.g. Villa et al., 2023) and compressional velocity (through Rayleigh wave ellipticity, e.g. Lin et al., 2012) structure. These parameters will effectively reconstruct the Green's functions with finer detail, which are crucial for accurate ground motion predictions (e.g. Moschetti et al., 2017) and deterministic seismic hazard assessment scenarios (e.g. Graves et al., 2011).

While ambient-noise cross-correlations are powerful to conduct surface wave tomography, the use of auto-correlations possesses the potential to image reflectors below each station in an essence similarly to techniques such as Receiver Functions and active source imaging. In specific, it has been proven practically (Zou and Clayton, 2024) that the auto-correlation function, after removing a spatially consistent source term, displays the ability to capture reflections below each station even in complex volcanic settings (e.g. Heath et al., 2018). Bi-material interface

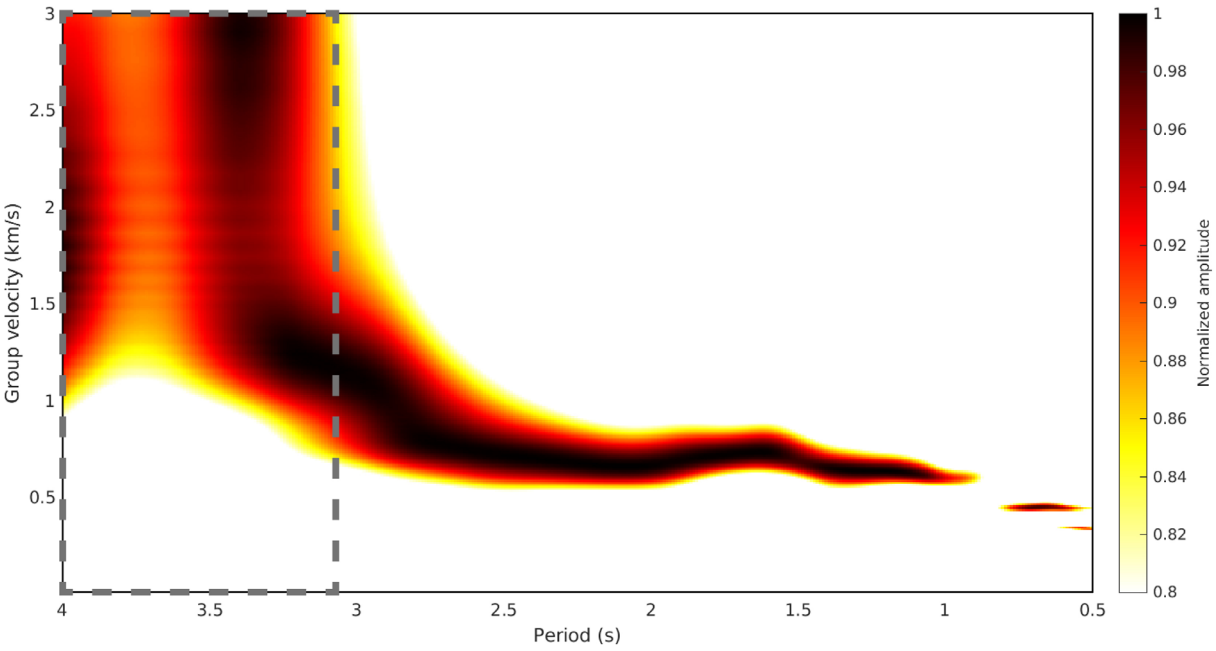

Figure 9. Example Frequency-Time Analysis (FTAN) diagram for the T-T cross-correlation (dominated by the Love wave dispersion) between virtual source stations STA20 and STA25 (locations depicted in Fig. 2b), band-passed near different central periods. Energies below 80% of the normalized envelope function at each period are not shown. Dashed rectangle outlines the periods where the dispersion curve is ambiguous.

impedance contrast and ambient-noise energetic frequency content are innate factors controlling the analysis. The results are expected to identify the exhibited fundamental period (Fig. 7) independently from the HVSR curves (e.g. Figs. 4 and 6) by single or multiple reflections. Complementary information from both datasets will reduce uncertainties in inverting for layer thickness, especially if we consider reflection multiples. We plan to utilize all stations deployed in Santorini from the current and previous experiments to better understand the shallow volcanic layer thickness and draw conclusions about past volcanic eruptions and the volcano behaviour in the future.

4. Conclusions

The deployment and operation of SantoArray was completed successfully. The relatively rapid emergency response to the earthquake swarm crisis among with the instrument and data retrieval rates underscore the potential of future large-N seismic experiments of similar nature in Greece and worldwide. Additional inter-disciplinary approaches are planned using SantoArray data. These efforts aim to enhance Santorini's seismic structure, study of the 2025 Santorini-Amorgos earthquake swarm and investigate the volcano's structure and behaviour. The new dataset provides excellent academic research setting for the dense tracking of the surface wave propagation and different ambient-noise tomography methodologies testing and development.

The indicative data usage examples presented previously, suggest that the SantoArray network offers a unique opportunity for determining the focal parameters of intra-caldera earthquakes, as the high-quality arrivals recorded by this dense network substantially improve hypocentral location errors. Moreover, the large number of waveform recordings from SantoArray enables the application of waveform cross-correlation techniques to estimate differential phase arrival times, which can be used for even more precise earthquake relocation – an especially valuable capability in such complex volcanic environments.

The SantoArray and particularly the inclusion of Phase II data will contribute to a better understanding of the complex volcanic structures, and particularly the areas of very high ground amplification. In addition, this dataset can be utilized for body-wave tomography, allowing the resolution of both low- and high-velocity anomalies with greater detail. This will enable the generation of high-resolution images of the internal structure of the Santorini volcanic complex, significantly enhancing our understanding of its subsurface characteristics. Moreover, the hybrid geometry of the network will also allow us to use the recorded ambient noise records for several purposes, such as noise autocorrelation, or to compute and use thousands of inter-station pairs for ambient noise cross-correlation tomography, yielding tomographic images of Santorini with unprecedented resolution.

Data availability statement. SantoArray station data and metadata will be archived soon to FDSN services (temporary station code: ZN) under an embargo status until funding acquisition and publishing of formal scientific results are concluded. Parties interested in data analysis beforehand can submit a reasonable request. Seismic records for the permanent Hellenic Unified Seismological Network were acquired from the HL (National Observatory of Athens, Institute of Geodynamics, Athens, 1975), HT (Aristotle University of Thessaloniki, 1981), and HA (University of Athens, 2008) networks, accessed through the National Observatory of Athens (NOA) EIDA node (Evangelidis et al., 2021).

Acknowledgements. We are thankful to the people from both institutes who have worked during these last few months towards making this experiment happen. We would also like to thank the technicians of the IRIS local technical company who participated in the field work, Manolis Pitsikalis, Ioanna Vamvakouri and other anonymous volunteers for providing local support, as well as the Institute for the Study and Monitoring of Santorini Volcano (ISMOSAV) for covering part of the installation costs. This work was supported by a subsidy from the Polish Ministry of Education and Science for the Institute of Geophysics, Polish Academy of Sciences.

References

Aristotle University of Thessaloniki, Aristotle University of Thessaloniki Seismological Network (1981). doi:10.7914/SN/HT.

Autumn, K. R., E. E. Hooft and D. R. Toomey (2025). Exploring Mid-to-Lower Crustal Magma Plumbing of Santorini and Kolumbo Volcanoes using PmP Tomography, Authorea Preprints.

Bohnhoff, M., M. Rische, T. Meier, D. Becker et al. (2006). Microseismic activity in the Hellenic Volcanic Arc, Greece, with emphasis on the seismotectonic setting of the Santorini-Amorgos zone, Tectonophysics, 423, 1-4, 17-33, doi:10.1016/j.tecto.2006.03.024.

Brenguier, F., P. Kowalski, N. Ackerley, N. Nakata et al. (2016). Toward 4D noise-based seismic probing of volcanoes: Perspectives from a large-N experiment on Piton de la Fournaise Volcano, Seismol. Res. Lett., 87, 1, 15-25, doi:10.1785/0220150173.

Brocher, T. M. (2005). Empirical relations between elastic wavespeeds and density in the Earth's crust, Bull. Seismol. Soc. Am., 95, 6, 2081-2092, doi:10.1785/0120050077.

Brüstle, A., W. Friederich, T. Meier and C. Gross (2014). Focal mechanism and depth of the 1956 Amorgos twin earthquakes from waveform matching of analogue seismograms, Solid Earth, 5, 2, 1027-1044, doi:10.5194/se-5-1027-2014.

Caputo, M., G. F. Panza and D. Postpischl (1970). Deep structure of the Mediterranean basin, J. Geophys. Res., 75, 26, 4919-4923.

Chatzis, N., C. Papazachos, N. Theodoulidis, P. Hatzidimitriou et al. (2022). Metamorphic bedrock geometry of Santorini using HVSR information and geophysical modeling of ambient noise and active-source surface-wave data, J. Volcanol. Geoth. Res., 432, 107692, doi:10.1016/j.jvolgeores.2022.107692.

Dimitriadis, I., C. Papazachos, D. Panagiotopoulos, P. Hatzidimitriou et al. (2010). P and S velocity structures of the Santorini-Coloumbo volcanic system (Aegean Sea, Greece) obtained by non-linear inversion of travel times and its tectonic implications, J. Volcanol. Geoth. Res., 195, 1, 13-30, doi:10.1016/j.jvolgeores.2010.05.013.

Dougherty, S. L., E. S. Cochran and R. M. Harrington (2019). The Large-N seismic survey in Oklahoma (LASSO) experiment, Seismol. Res. Lett., 90, 5, 2051-2057, doi:10.1785/0220190094.

Druitt, T. H., F. W. McCoy and G. E. Vougioukalakis (2019). The Late Bronze Age Eruption of Santorini Volcano and its Impact on the Ancient Mediterranean World, Elements, 15, 3, 185-190, doi:10.2138/gselements.15.3.185.

Druitt, T. H., L. Edwards, R. M. Mellors, D. M. Pyle et al. (1999). Santorini volcano, Geol. Soc. Mem., 19, doi:10.1144/GSL.MEM.1999.019.01.12.

Ehrlich, Y., L. Regev and E. Boaretto (2021). Discovery of annual growth in a modern olive branch based on carbon isotopes and implications for the Bronze Age volcanic eruption of Santorini, Sci. Rep., 11, 1, 1-11, doi:10.1038/s41598-020-79024-4.

Evangelidis, C. P., N. Triantafyllis, M. Samios, K. Boukouras et al. (2021). Seismic waveform data from Greece and Cyprus: Integration, archival and open access, Seismol. Soc. Am., 92, 3, 1672-1684, doi:10.1785/0220200408.

Flaherty, T., T. H. Druitt, H. Tuffen, M. D. Higgins et al. (2018). Multiple timescale constraints for high-flux magma chamber assembly prior to the Late Bronze Age eruption of Santorini (Greece), Contrib. Mineral. Petrol., 173, 1-21, doi:10.1007/s00410-018-1490-1.

Foumelis, M., E. Trasatti, E. Papageorgiou, S. Stramondo et al. (2013). Monitoring Santorini volcano (Greece) breathing from space, Geoph. J. Int., 193, 1, 161-170, doi:10.1093/gji/ggs135.

Fountoulakis, I. and C. P. Evangelidis (2025). The 2024-2025 seismic sequence in the Santorini-Amorgos region: Insights into volcano-tectonic activity through high-resolution seismic monitoring, Seismica, 4, 1, doi:10.26443/seismica.v4i1.1663.

Fytikas, M., F. Innocenti, P. Manetti, A. Peccerillo et al. (1984). Tertiary to Quaternary evolution of volcanism in the Aegean region, Geol. Soc. Spec. Publ., 17, 1, 687-699, doi:10.1144/GSL.SP.1984.017.01.55.

Georgalas, G. (1953). L'éruption du volcan de Santorini en 1950, Bull. Volcanol., 13, 39-55.

Gkogkas, K., F. C. Lin, A. A. Allam and Y. Wang (2021). Shallow Damage Zone Structure of the Wasatch Fault in Salt Lake City from Ambient-Noise Double Beamforming with a Temporary Linear Array, Seismol. Res. Lett., doi:10.1785/0220200404.

Graves, R. W., B. T. Aagaard and K. W. Hudnut (2011). The ShakeOut earthquake source and ground motion simulations, Earthq. Spectra, 27, 2, 273-291, doi:10.1193/1.3570677.

Hannemann, K., C. Papazachos, M. Ohrnberger, A. Savvaidis et al. (2014). Three-dimensional shallow structure from high-frequency ambient noise tomography: New results for the Mygdonia basin-Euroseistest area, northern Greece, J. Geophys. Res., Solid Earth, 119, 4979-4999, doi:10.1002/2013JB010914.

Heath, B. A., E. E. E. Hooft and D. R. Toomey (2018). Autocorrelation of the seismic wavefield at Newberry Volcano: Reflections from the magmatic and geothermal systems, Geophys. Res. Lett., doi:10.1002/2017GL076706.

Heath, B. A., E. E. E. Hooft, D. R. Toomey, C. B. Papazachos et al. (2019). Tectonism and its relation to magmatism around Santorini volcano from upper crustal P wave velocity, J. Geophys. Res., Solid Earth, 124, 10610-10629, doi:10.1029/2019JB017699.

Hooft, E. E. E., B. A. Heath, D. R. Toomey, M. Paulatto et al. (2019). Seismic imaging of Santorini: Subsurface constraints on caldera collapse and present-day magma recharge, Earth Planet. Sci. Lett., 514, 48-61, doi:10.1016/j.epsl.2019.02.033.

Hooft, E. E. E., P. Nomikou, D. R. Toomey, D. Lampridou et al. (2017). Backarc tectonism, volcanism, and mass wasting shape seafloor morphology in the Santorini-Christiana-Amorgos region of the Hellenic Volcanic Arc, Tectonophysics, 712-713, 396-414, doi:10.1016/j.tecto.2017.06.005.

Hufstetler, R. S., E. E. Hooft, D. R. Toomey, B. P. VanderBeek et al. (2025). Seismic Structure of the Mid to Upper Crust at the Santorini-Kolumbo Magma System from Joint Earthquake and Active Source Vp-Vs Tomography, Geochem. Geophys. Geosyst., 26, 4, e2024GC012022, doi:10.1029/2024GC012022.

Isken, M. P., J. Karstens, P. Nomikou, M. M. Parks et al. (2025). Volcanic crisis reveals coupled magma system at Santorini and Kolumbo, Nature, 645, 8082, 939-945, doi:10.1038/s41586-025-09525-7.

Konstantinou, K. I. (2010). Crustal rheology of the Santorini-Amorgos zone: Implications for the nucleation depth and rupture extent of the 9 July 1956 Amorgos earthquake, southern Aegean, J. Geodyn., 50, 400-409, doi:10.1016/j.jog.2010.05.002.

Klein, F. W. (2002). User's Guide to HYPOINVERSE-2000, a Fortran Program to Solve for Earthquake Locations and Magnitudes, U. S. Geol. Surv. Open File Rep., 02-171, 123, doi:10.3133/ofr02171.

Le Pichon, X. and J. Angelier (1979). The Hellenic arc and trench system: a key to the neotectonic evolution of the eastern Mediterranean area, Tectonophysics, 60, 1-2, 1-42, doi:10.1016/0040-1951(79)90131-8.

Lin, F. C., B. Schmandt and V. C. Tsai (2012). Joint inversion of Rayleigh wave phase velocity and ellipticity using USArray: constraining velocity and density structure in the upper crust, Geophys. Res. Letts., 39, L12303, doi:10.1029/2012GL052196.

McVey, B. G., E. E. E. Hooft, B. A. Heath, D. R. Toomey et al. (2020). Magma accumulation beneath Santorini volcano, Greece, from P-wave tomography, Geology, 48, 3, 231-235, doi:10.1130/G47127.1.

Moschetti, M. P., S. Hartzell, L. Ramírez-Guzmán, A. D. Frankel et al. (2017). 3D ground-motion simulations of Mw 7 earthquakes on the Salt Lake City segment of the Wasatch fault zone: Variability of long-period ($T \geq 1$ s) ground motions and sensitivity to kinematic rupture parameters, Bull. Seismol. Soc. Am., 107, 4, 1704-1723, doi:10.1785/0120160307.

Nakamura, Y. (1989). A method for dynamic characteristics estimation of subsurface using microtremor on the ground surface, Railway Technical Research Institute, Quarterly Reports, 30, 1.

National Observatory of Athens, Institute of Geodynamics, Athens (1975). Hellenic Unified Seismological Network, Data set, International Federation of Digital Seismograph Networks, doi:10.7914/SN/HL.

Newman, A. V., S. Stiros, L. Feng, P. Psimoulis et al. (2012). Recent geodetic unrest at Santorini Caldera, Greece, Geophys. Res. Lett., 39, L06309, doi:10.1029/2012GL051286.

Nomikou, P., C. Hübscher, D. Papanikolaou, G. P. Farangitakis et al. (2018). Expanding extension, subsidence and lateral segmentation within the Santorini-Amorgos basins during Quaternary: Implications for the 1956 Amorgos events, central-south Aegean Sea, Greece, Tectonophysics, 722, 138-153, doi:10.1016/j.tecto.2017.10.016.

Okal, E. A., C. E. Synolakis, B. Uslu, N. Kalligeris et al. (2009). The 1956 earthquake and tsunami in Amorgos, Greece, Geophys. J. Int., 178, 1533-1554, doi:10.1111/j.1365-246X.2009.04237.x.

Papadimitriou, P., V. Kapetanidis, A. Karakonstantis, G. Kaviris et al. (2015). The Santorini Volcanic Complex: A detailed multi-parameter seismological approach with emphasis on the 2011-2012 unrest period, J. Geodyn. 85, 32-57, doi:10.1016/j.jog.2014.12.004.

Papadopoulos, G. A. and S. B. Pavlides (1992). The large 1956 earthquake in the South Aegean: Macroseismic field configuration, faulting, and neotectonics of Amorgos Island, Earth Planet. Sci. Lett. 113, 383-396, doi:10.1016/0012-821X(92)90140-Q.

Papazachos, B. C. and P. E. Comninakis (1971). Geophysical and tectonic features of the Aegean arc, J. Geophys. Res., 76, 35, 8517-8533, doi:10.1029/JB076i035p08517.

Papazachos, B. and C. Papazachou (2003). The Earthquakes of Greece, Ziti Publ. Thessaloniki, Greece, 286, in Greek.

Papazachos, B. C. and P. E. Comninakis (1969). Geophysical features of the Greek island arc and the Eastern Mediterranean ridge, Comptes Rendu des Séances de la Conférence Réunie à Madrid, 16, 74-75.

Papazachos, C. B. (2019). Deep Structure and Active Tectonics of the South Aegean Volcanic Arc, Elements, 15, 3, 153-158, doi:10.2138/gselements.15.3.153.

Papazachos, C., M. Foumelis, S. Bitharis, Ch. Pikridas et al. (2025). The Santorini 2024-25 volcano-tectonic sequence: Constraining the initial phase of the intra-caldera unrest, Geophy. Res. Lett., 52, 13, doi:10.1029/2025GL115856.

Parks, M. M., J. D. Moore, X. Papanikolaou, J. Biggs et al. (2015). From quiescence to unrest: 20 years of satellite geodetic measurements at Santorini volcano, Greece, J. Geoph. Res., Solid Earth, 120, 2, 1309-1328, doi:10.1002/2014JB011540.

Parks, M. M., S. Caliro, G. Chiodini, D. M. Pyle et al. (2013). Distinguishing contributions to diffuse CO_2 emissions in volcanic areas from magmatic degassing and thermal decarbonation using soil gas ^{222}Rn-δ^{13}C systematics: application to Santorini volcano, Greece, Earth Planet. Sci. Lett., 377-378, 180-190, doi:10.1016/j.epsl.2013.06.046.

Pyle, D. M. and J. R. Elliott (2006). Quantitative morphology, recent evolution, and future activity of the Kameni Islands volcano, Santorini, Greece, Geosphere, 2, 5, 253-268, doi:10.1130/GES00028.1.

Skarpelis, N. and A. Liati (1990). The prevolcanic basement of Thera at Athinios: Metamorphism. Plutonism and mineralization, in Thera and the Aegean World III, 2, D. A. Hardy (Ed.), The Thera Foundation, London, 172-182.

Tassi, F., O. Vaselli, C. B. Papazachos, L. Giannini et al. (2013). Geochemical and isotopic changes in the fumarolic and submerged gas discharges during the 2011-2012 unrest at Santorini caldera (Greece), Bull. Volcanol., 75, 711, doi:10.1007/s00445-013-0711-8.

Tsampouraki-Kraounaki, K., D. Sakellariou, G. Rousakis, I. Morfis et al. (2021). The Santorini-Amorgos shear zone: Evidence for dextral transtension in the south Aegean back-arc region, Greece, Geosciences, 11, 5, 216, doi:10.3390/geosciences11050216.

Tzanis, A., S. Chailas, V. Sakkas and E. Lagios (2020). Tectonic deformation in the Santorini volcanic complex (Greece) as inferred by joint analysis of gravity, magnetotelluric and DGPS observations, Geophys. J. Int., 220, 1, 461-489, doi:10.1093/gji/ggz461.

University of Athens (2008). Hellenic Seismological Network, University of Athens, Seismological Laboratory, doi:10.7914/SN/HA.

Uyeda, S. and H. Kanamori (1979). Back-arc opening and the mode of subduction, J. Geophys. Res., Solid Earth, 84, B3, 1049-1061.

Villa, V., Y. Li, R. W. Clayton and P. Persaud (2023), Three-Dimensional Basin Depth Map of the Northern Los Angeles from Gravity and Seismic Measurements, J. Geophys. Res., Solid Earth, 128, e2022JB025425.

Vougioukalakis, G. and M. Fytikas (2005). Volcanic hazards in the Aegean area, relative risk evaluation, monitoring and present state of the active volcanic centers, in The South Aegean Active Volcanic Arc – Present Knowledge and Future Perspectives M. Fytikas and G. Vougioukalakis (Eds.), Elsevier Series Developments in Volcanology, 7, 161-183, doi:10.1016/S1871-644X(05)80037-3.

Wang, Y., F. C. Lin, B. Schmandt and J. Farrell (2017). Ambient noise tomography across Mount St. Helens using a dense seismic array, J. Geophys. Res., Solid Earth, 122, doi:10.1002/2016JB013769.

Wathelet, M., J. L. Chatelain, C. Cornou, G. Di Giulio et al. (2020). Geopsy: A User-Friendly Open-Source Tool Set for Ambient Vibration Processing, Seismol. Res. Lett., 91, 3, 1878-1889, doi:10.1785/0220190360.

Yao, H., R. D. van Der Hilst and M. V. De Hoop (2006). Surface-wave array tomography in SE Tibet from ambient seismic noise and two-station analysis-I, Phase velocity maps, Geophys. J. Int., 166, 2, 732-744, doi:10.1111/j.1365-246X.2006.03028.x.

Zou, C. and R. Clayton (2024). Imaging the Northern Los Angeles Basins with Autocorrelations, Seismol. Res. Lett., 96, 3, 1791-1801, doi:10.1785/0220240140.

***CORRESPONDING AUTHOR: Konstantinos GKOGKAS**,
Institute of Geophysics, Warsaw, Poland
email: konstantinos.gkogkas@igf.edu.pl